

Volumetric imaging and quantification of cytoarchitecture and myeloarchitecture with intrinsic scattering contrast

Conor Leahy, Harsha Radhakrishnan, and Vivek J. Srinivasan*

Biomedical Engineering Department, University of California Davis, Davis, CA 95616, USA
*vsriniv@ucdavis.edu

Abstract: We present volumetric imaging and computational techniques to quantify neuronal and myelin architecture with intrinsic scattering contrast. Using spectral / Fourier domain Optical Coherence Microscopy (OCM) and software focus-tracking we validate imaging of neuronal cytoarchitecture and demonstrate quantification in the rodent cortex *in vivo*. Additionally, by *ex vivo* imaging in conjunction with optical clearing techniques, we demonstrate that intrinsic scattering contrast is preserved in the brain, even after sacrifice and fixation. We volumetrically image cytoarchitecture and myeloarchitecture *ex vivo* across the entire depth of the rodent cortex. Cellular-level imaging up to the working distance of our objective (~3 mm) is demonstrated *ex vivo*. Architectonic features show the expected laminar characteristics; moreover, changes in contrast after the application of acetic acid suggest that entire neuronal cell bodies are responsible for the “negative contrast” present in the images. Clearing and imaging techniques that preserve tissue architectural integrity have the potential to enable non-invasive studies of the brain during development, disease, and remodeling, even in samples where exogenous labeling is impractical.

©2013 Optical Society of America

OCIS codes: (110.4500) Optical coherence tomography; (170.3880) Medical and biological imaging; (290.1350) Backscattering; (170.0180) Microscopy; (170.6900) Three-dimensional microscopy.

References and links

1. K. A. Kasischke, H. D. Vishwasrao, P. J. Fisher, W. R. Zipfel, and W. W. Webb, “Neural activity triggers neuronal oxidative metabolism followed by astrocytic glycolysis,” *Science* **305**(5680), 99–103 (2004).
2. D. A. Dombeck, K. A. Kasischke, H. D. Vishwasrao, M. Ingelsson, B. T. Hyman, and W. W. Webb, “Uniform polarity microtubule assemblies imaged in native brain tissue by second-harmonic generation microscopy,” *Proc. Natl. Acad. Sci. U.S.A.* **100**(12), 7081–7086 (2003).
3. M. J. Farrar, F. W. Wise, J. R. Fetcho, and C. B. Schaffer, “In vivo imaging of myelin in the vertebrate central nervous system using third harmonic generation microscopy,” *Biophys. J.* **100**(5), 1362–1371 (2011).
4. Y. Fu, T. B. Huff, H. W. Wang, H. Wang, and J. X. Cheng, “Ex vivo and in vivo imaging of myelin fibers in mouse brain by coherent anti-Stokes Raman scattering microscopy,” *Opt. Express* **16**(24), 19396–19409 (2008).
5. S. Witte, A. Negrean, J. C. Lodder, C. P. de Kock, G. Testa Silva, H. D. Mansvelder, and M. Louise Groot, “Label-free live brain imaging and targeted patching with third-harmonic generation microscopy,” *Proc. Natl. Acad. Sci. U.S.A.* **108**(15), 5970–5975 (2011).
6. J. Ben Arous, J. Binding, J. F. Léger, M. Casado, P. Topilko, S. Gigan, A. C. Boccara, and L. Bourdieu, “Single myelin fiber imaging in living rodents without labeling by deep optical coherence microscopy,” *J. Biomed. Opt.* **16**(11), 116012 (2011).
7. V. J. Srinivasan, H. Radhakrishnan, J. Y. Jiang, S. Barry, and A. E. Cable, “Optical coherence microscopy for deep tissue imaging of the cerebral cortex with intrinsic contrast,” *Opt. Express* **20**(3), 2220–2239 (2012).
8. O. Assayag, K. Grieve, B. Devaux, F. Harms, J. Pallud, F. Chretien, C. Boccara, and P. Varlet, “Imaging of non-tumorous and tumorous human brain tissues with full-field optical coherence tomography,” *NeuroImage. Clinical* **2**, 549–557 (2013).
9. M. Snuderl, D. Wirth, S. A. Sheth, S. K. Bourne, C. S. Kwon, M. Ancukiewicz, W. T. Curry, M. P. Frosch, and A. N. Yaroslavsky, “Dye-enhanced multimodal confocal imaging as a novel approach to intraoperative diagnosis of brain tumors,” *Brain Pathol.* **23**(1), 73–81 (2013).

10. H. Wang, A. J. Black, J. Zhu, T. W. Stigen, M. K. Al-Qaisi, T. I. Netoff, A. Abosch, and T. Akkin, "Reconstructing micrometer-scale fiber pathways in the brain: multi-contrast optical coherence tomography based tractography," *Neuroimage* **58**(4), 984–992 (2011).
11. H. Hama, H. Kurokawa, H. Kawano, R. Ando, T. Shimogori, H. Noda, K. Fukami, A. Sakaue-Sawano, and A. Miyawaki, "Scale: a chemical approach for fluorescence imaging and reconstruction of transparent mouse brain," *Nat. Neurosci.* **14**(11), 1481–1488 (2011).
12. Y. He and R. K. Wang, "Dynamic optical clearing effect of tissue impregnated with hyperosmotic agents and studied with optical coherence tomography," *J. Biomed. Opt.* **9**(1), 200–206 (2004).
13. F. Helmchen and W. Denk, "Deep tissue two-photon microscopy," *Nat. Methods* **2**(12), 932–940 (2005).
14. J. A. Izatt, M. R. Hee, G. M. Owen, E. A. Swanson, and J. G. Fujimoto, "Optical coherence microscopy in scattering media," *Opt. Lett.* **19**(8), 590–592 (1994).
15. P. S. Tsai, J. P. Kaufhold, P. Blinder, B. Friedman, P. J. Drew, H. J. Karten, P. D. Lyden, and D. Kleinfeld, "Correlations of Neuronal and Microvascular Densities in Murine Cortex Revealed by Direct Counting and Colocalization of Nuclei and Vessels," *J. Neurosci.* **29**(46), 14553–14570 (2009).
16. R. A. Drezek, T. Collier, C. K. Brookner, A. Malpica, R. Lotan, R. R. Richards-Kortum, and M. Follen, "Laser scanning confocal microscopy of cervical tissue before and after application of acetic acid," *Am. J. Obstet. Gynecol.* **182**(5), 1135–1139 (2000).
17. T. Collier, P. Shen, B. de Pradier, K. B. Sung, R. Richards-Kortum, M. Follen, and A. Malpica, "Near real time confocal microscopy of amelanotic tissue: dynamics of aceto-whitening enable nuclear segmentation," *Opt. Express* **6**(2), 40–48 (2000).
18. A. F. McCaslin, B. R. Chen, A. J. Radosevich, B. Cauli, and E. M. Hillman, "In vivo 3D morphology of astrocyte-vasculature interactions in the somatosensory cortex: implications for neurovascular coupling," *J. Cereb. Blood Flow Metab.* **31**(3), 795–806 (2011).
19. T. S. Skoglund, R. Pascher, and C. H. Berthold, "Heterogeneity in the columnar number of neurons in different neocortical areas in the rat," *Neurosci. Lett.* **208**(2), 97–100 (1996).
20. D. J. Faber, F. J. van der Meer, M. C. G. Aalders, and T. van Leeuwen, "Quantitative measurement of attenuation coefficients of weakly scattering media using optical coherence tomography," *Opt. Express* **12**(19), 4353–4365 (2004).
21. K. Chung, J. Wallace, S. Y. Kim, S. Kalyanasundaram, A. S. Andalman, T. J. Davidson, J. J. Mirzabekov, K. A. Zalocusky, J. Mattis, A. K. Denisin, S. Pak, H. Bernstein, C. Ramakrishnan, L. Grose, V. Gradinaru, and K. Deisseroth, "Structural and molecular interrogation of intact biological systems," *Nature* **497**(7449), 332–337 (2013).
22. K. Chung and K. Deisseroth, "CLARITY for mapping the nervous system," *Nat. Methods* **10**(6), 508–513 (2013).
23. M. T. Ke, S. Fujimoto, and T. Imai, "SeeDB: a simple and morphology-preserving optical clearing agent for neuronal circuit reconstruction," *Nat. Neurosci.* **16**(8), 1154–1161 (2013).
24. M. Rieckher, U. J. Birk, H. Meyer, J. Ripoll, and N. Tavernarakis, "Microscopic optical projection tomography in vivo," *PLoS ONE* **6**(4), e18963 (2011).
25. A. L. Pistorio, S. H. Hendry, and X. Wang, "A modified technique for high-resolution staining of myelin," *J. Neurosci. Methods* **153**(1), 135–146 (2006).
26. W. Denk and H. Horstmann, "Serial block-face scanning electron microscopy to reconstruct three-dimensional tissue nanostructure," *PLoS Biol.* **2**(11), e329 (2004).
27. W. Denk, K. L. Briggman, and M. Helmstaedter, "Structural neurobiology: missing link to a mechanistic understanding of neural computation," *Nat. Rev. Neurosci.* **13**(5), 351–358 (2012).
28. J. W. Bohland, C. Wu, H. Barbas, H. Bokil, M. Bota, H. C. Breiter, H. T. Cline, J. C. Doyle, P. J. Freed, R. J. Greenspan, S. N. Haber, M. Hawrylycz, D. G. Herrera, C. C. Hilgetag, Z. J. Huang, A. Jones, E. G. Jones, H. J. Karten, D. Kleinfeld, R. Kötter, H. A. Lester, J. M. Lin, B. D. Mensh, S. Mikula, J. Panksepp, J. L. Price, J. Saffdieh, C. B. Saper, N. D. Schiff, J. D. Schmahmann, B. W. Stillman, K. Svoboda, L. W. Swanson, A. W. Toga, D. C. Van Essen, J. D. Watson, and P. P. Mitra, "A proposal for a coordinated effort for the determination of brainwide neuroanatomical connectivity in model organisms at a mesoscopic scale," *PLoS Comput. Biol.* **5**(3), e1000334 (2009).
29. A. Burkhalter and K. L. Bernardo, "Organization of corticocortical connections in human visual cortex," *Proc. Natl. Acad. Sci. U.S.A.* **86**(3), 1071–1075 (1989).
30. O. O. Ahsen, Y. K. Tao, B. M. Potsaid, Y. Sheikine, J. Jiang, I. Grulkowski, T.-H. Tsai, V. Jayaraman, M. F. Kraus, J. L. Connolly, J. Hornegger, A. Cable, and J. G. Fujimoto, "Swept source optical coherence microscopy using a 1310 nm VCSEL light source," *Opt. Express* **21**(15), 18021–18033 (2013).
31. M. Hawrylycz, R. A. Baldock, A. Burger, T. Hashikawa, G. A. Johnson, M. Martone, L. Ng, C. Lau, S. D. Larson, J. Nissanov, L. Puelles, S. Ruffins, F. Verbeek, I. Zaslavsky, and J. Boline, "Digital atlasing and standardization in the mouse brain," *PLoS Comput. Biol.* **7**(2), e1001065 (2011).
32. C. Schmitz and P. R. Hof, "Design-based stereology in neuroscience," *Neuroscience* **130**(4), 813–831 (2005).
33. T. Ragan, L. R. Kadiri, K. U. Venkataraju, K. Bahlmann, J. Sutin, J. Taranda, I. Arganda-Carreras, Y. Kim, H. S. Seung, and P. Osten, "Serial two-photon tomography for automated ex vivo mouse brain imaging," *Nat. Methods* **9**(3), 255–258 (2012).

1. Introduction

Label-free volumetric optical microscopy has many advantages over conventional histology and light microscopy, including sample preservation and the capability to image endogenous contrast. Several label-free microscopic techniques have been used to image intrinsic contrast in thick brain tissues. Two-photon microscopy images the spatial distribution of intrinsic fluorophores such as NADH [1]. Second harmonic generation is sensitive to polarized microtubules [2]. Third-harmonic generation [3] and coherent anti-Stokes Raman scattering microscopy [4] have been demonstrated to image myelin based on its structural and biochemical properties, respectively. Third-harmonic generation also visualizes neuronal cell bodies due to lack of structural phase matching [5]. Elastic backscattering techniques such as Optical Coherence Microscopy (OCM) and confocal reflectance microscopy provide contrast comparable to third-harmonic generation in brain tissue, depicting both neuronal cell bodies and myelinated axons [6–9]. The birefringent properties of the myelin sheath can be interrogated with polarization-sensitive imaging to provide additional contrast [10].

Advances in optical clearing methods have recently provided the transparency necessary for deep tissue imaging of fluorescence over previously unattainable depths in the mouse brain [11]. While it may at first seem counterintuitive that a scattering-based technique such as OCM could benefit from optical clearing, there is a precedent for hyperosmotic agents changing the refractive index distribution and improving reflectance-based contrast in cells and tissues [12]. Moreover, for deep tissue two-photon fluorescence brain imaging, scattering limits the imaging depth [13]; therefore a reduction in scattering may improve imaging depth. However, backscattering is also responsible for OCM image contrast, thus elimination of scattering would also eliminate useful sources of contrast. Nevertheless, the high sensitivity of OCM to small back-reflections on the order of -100 dB [14] suggests that lowering overall scattering may be beneficial, even if the cost is a reduction in signal levels. Thus, there is ample rationale to investigate the potential benefits of refractive index matching induced by optical clearing, although clearing may be a “double-sided sword” for reflectance-based imaging.

In this work, through a combination of *ex vivo* and *in vivo* studies, we apply and validate OCM for volumetric and quantitative imaging of cytoarchitecture and myeloarchitecture in the rodent brain. Furthermore, we show that image contrast and imaging depth can be modulated through different chemical treatments. These label-free and volumetric imaging methods have numerous potential applications in brain research [15].

2. Methods

2.1 OCM system description and software focus-tracking

A spectral/Fourier domain OCM microscope was constructed on a Nikon microscope platform with a central wavelength of 1310 nm for imaging cortical tissue. The light source consisted of two unpolarized superluminescent diodes combined using a 50 / 50 fiber coupler to yield a bandwidth of 160 nm. The axial (depth) resolution was 4.7 μm in air (3.5 μm in tissue). A spectrometer with a 1024 pixel InGaAs line scan camera operated at 47,000 axial scans per second. For OCM imaging, a 40x water immersion objective (Olympus LUMPLANFL/IR 40X W, NA 0.8) achieved a transverse resolution of 0.9 microns (full-width at half-maximum of the intensity profile). The sensitivity was approximately 100 dB. Further details of the system have been previously reported [7].

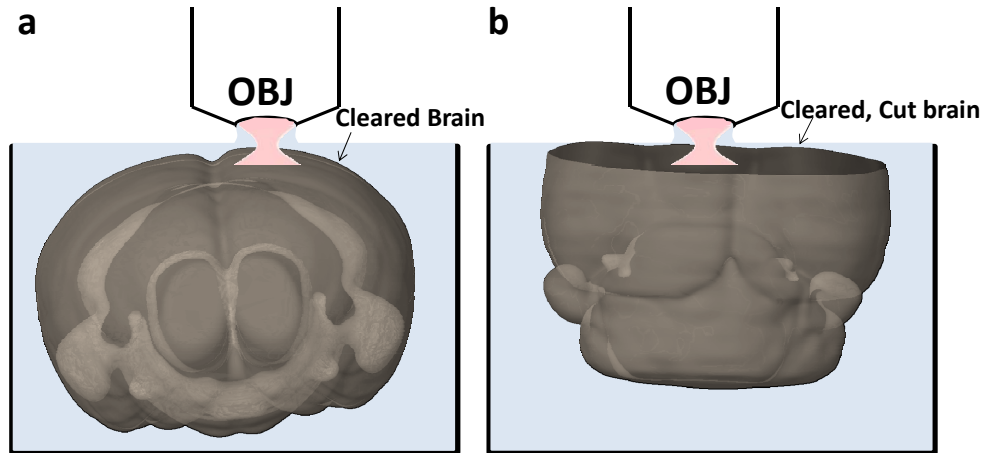


Fig. 1. Geometries for *ex vivo* brain imaging. Imaging was performed in an optically cleared brain, via the intact cortical surface (a), or via a cut coronal plane (b). The mouse brain for this figure was rendered using Brain Explorer 2 software (<http://mouse.brain-map.org/static/brainexplorer>). (OBJ – objective lens)

For imaging, the sample arm assembly was initially set so that the optical focus was just above the cortical surface. The sample arm assembly was then translated in increments of 5 microns. A three-dimensional data set was acquired at each focusing depth. Thus, a four-dimensional data set was generated, with dimensions corresponding to x position, y position, path length (z), and the sample arm assembly translation (Z). Z is used to denote a physical translation of the sample arm assembly, and z to denote the path length (group delay). The raw OCM data could thus be described as $A(x, y, z, Z)$, where A is the OCM signal amplitude at a particular (x, y, z) coordinate, corresponding to a particular sample arm assembly translation of Z . A fitting procedure [7] was used to determine the path length to the focus as a function of x, y , and Z , i.e., $z_{focus}(x, y, Z)$. The term $z(d_{brain}, Z)$ relates path length to a specific sample arm assembly translation and depth in the brain (d_{brain}). Then, averaging was performed using a weighting function, $w(z - z_{focus})$, which preferentially weighted path lengths near the focus:

$$\hat{A}(x, y, d_{brain}) = \sum_i w[z(d_{brain}, Z_i) - z_{focus}(x, y, Z_i)] A[x, y, z(d_{brain}, Z_i), Z_i] \quad (1)$$

In the above expression, $\hat{A}(x, y, d_{brain})$ represents the estimate of the local OCM signal amplitude, obtained from averaging data from multiple sample arm assembly translations. The averaging procedure is based on the insight that data that is slightly out of focus may contribute to speckle reduction without a severe resolution loss. This averaging was essential in yielding sufficiently high quality data to apply the quantitative metrics described below.

2.2 Two-photon microscopy

Two-photon microscopy (TPM) was performed prior to OCM imaging in rats on a separate microscope to determine the cell types visualized by OCM. TPM imaging was performed up to a depth of 300 microns after microinjection of OGB-1 using bolus loading to label neurons and astrocytes [12] and topical application of sulfurhodamine-101 (SR-101) to label astrocytes [13]. Data sets were co-registered and compared quantitatively.

2.3 Animal preparations

The animal procedures were approved by the Subcommittee on Research Animal Care where these experiments were performed. For the *in vivo* measurements, male Sprague-Dawley rats (300-320 g) or C57BL/6J mice (25-30 g) were used while the *ex vivo* images were obtained from brains of male C57BL/6 mice (25-30 g).

For *in vivo* OCM rat imaging, Sprague-Dawley rats (N = 2) were initially anesthetized with 2-2.5% v/v isoflurane with a gas mixture of 80% air and 20% oxygen. Tracheostomy for mechanical ventilation and cannulation of the femoral artery for blood pressure monitoring and the femoral vein for anesthetic administration were performed. Following catheterization, the animal was mounted on a stereotactic frame and a craniotomy was performed. A cranial window was created below the parietal bone, with the dura removed. The cranial window was filled with 1.5% agarose (Sigma MO USA), mixed in aCSF. Dental acrylic was used to seal the cranial window to the skull. To relieve excess intra-cerebral pressure, a ventriculostomy of the IVth ventricle was performed. Following the surgical procedures, the anesthesia was changed to alpha-chloralose (loading dose – 40 mg/kg; maintaining dose – 50 mg/kg/hr). During the imaging process, rats were ventilated with a mixture of air and O₂. Imaging was performed through the sealed cranial window, using distilled water as the immersion medium, as described previously [6, 7]. An intravenous bolus of pancuronium bromide (2 mg/kg) was administered followed by continuous intravenous infusion at 2 mg/kg/hr to minimize possible animal motion. Throughout the surgical and imaging procedures, the blood pressure was monitored via a transducer connected to the arterial cannula and the animal's core temperature was maintained at 37 degrees Celsius using a heating blanket. Blood gases were controlled within physiological limits.

For *in vivo* OCM mouse imaging, one C57BL/6J mouse (N = 1) was anesthetized with isoflurane (1-2% in a mixture of N₂O and O₂) through a nose cone and placed on a stereotaxic frame. After shaving and laterally reflecting the scalp, a midline craniectomy of 5 mm in diameter was carefully drilled under saline cooling to remove most of the frontal and parietal bones bilaterally. A closed cranial window was constructed using a glass coverslip, filled with phosphate-buffered saline, and sealed with dental cement. Imaging was performed through the sealed cranial window, using distilled water as the immersion medium. The blood pressure was monitored via a transducer connected to the arterial cannula and the animal's core temperature was maintained at 37 degrees Celsius using a heating blanket. Blood gases were controlled within physiological limits.

C57BL/6 mice were also used for *ex vivo* imaging of the cortical column (N = 2). The mice were perfused transcardially with 4% PFA/PBS. The extracted brains were then fixed in 4% PFA/PBS, cryoprotected, and optically cleared with *ScaleA2*, as previously reported [11]. The whole brain was immersed in the *ScaleA2* solution, which also formed the medium for the immersion objective during imaging, as shown in Fig. 1(a). In some experiments, the brain was cut along a coronal plane and imaged as shown in Fig. 1(b). Care was taken to ensure that the brain surface was perpendicular to the optic axis during microscopic imaging.

In order to investigate sources of image contrast, acetic acid was added to the *ScaleA2* solution. The effects of acetic acid, commonly used to aid in the detection of precancerous changes in the cervix, have been well-established from reflectance confocal microscopy [16, 17]. In particular, it has been shown that acetic acid increases scattering from cell nuclei due to nuclear coagulation.

2.4 Data processing

2.4.1 Cell detection

Neuronal cell bodies were segmented using an *in vivo* 600 μ m cubic OCM data set from the rat somatosensory cortex, resampled to contain 512 x 512 x 512 voxels. In order to quantify the neuronal cell bodies contained within the imaged volume, the data was first normalized to

impose a consistent signal level at each depth. A 3-D isotropic low-pass filter was then applied to the volume and further thresholded in order to segment the dark cell bodies from the surrounding tissue. This resulted in a binary map of the cell structures within the image volume. Cells comprising less than 50 voxels were discarded in an effort to mitigate noise. The binary volumetric map could then be rendered in three-dimensions. Each detected cell was labeled, and then localized by determining its centroid. The centroid of a given cell can be found by first computing the image moments, using the formula

$$M_{pqr} = \iiint x^p y^q z^r f(x, y, z) dx dy dz \quad (2)$$

where $f(x, y, z)$ is the cell binary map and M_{pqr} is the image moment. The co-ordinates $\{\bar{x}, \bar{y}, \bar{z}\}$ of the centroid are then given by

$$\{\bar{x}, \bar{y}, \bar{z}\} = \left\{ \frac{M_{100}}{M_{000}}, \frac{M_{010}}{M_{000}}, \frac{M_{001}}{M_{000}} \right\} \quad (3)$$

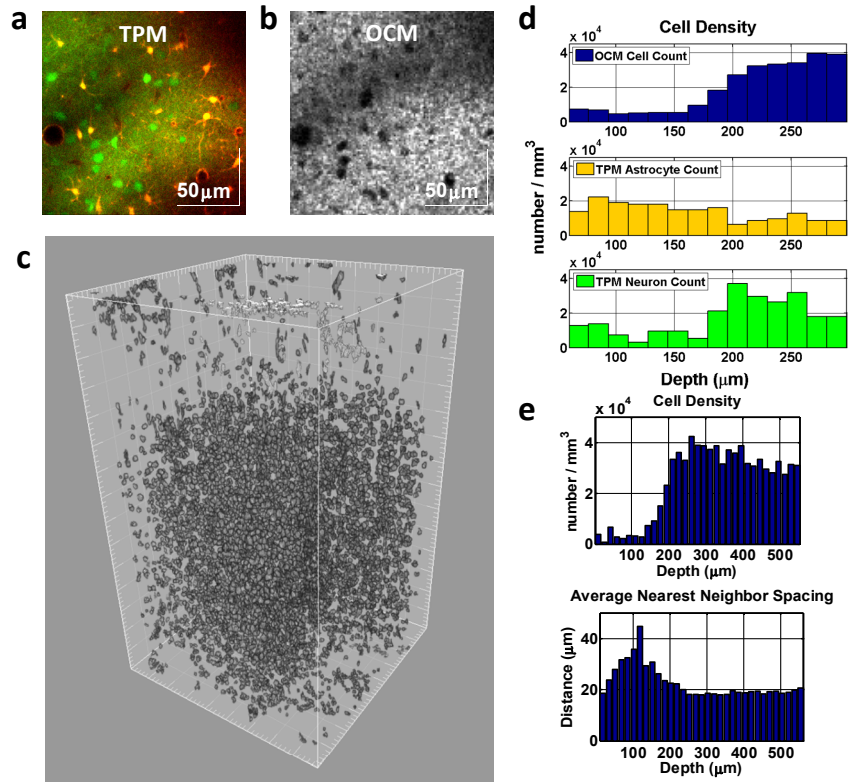


Fig. 2. OCM performs quantitative neuromorphometry *in vivo*. (a) Two-photon microscopy, after co-labeling with OGB-1 (green) and SR-101 (red), depicts neuronal cell bodies as green spherical regions labeled with OGB-1 but not SR-101. Astrocytes are labeled with both OGB-1 and SR-101 and hence appear orange. (b) Co-registered OCM of the same brain shows approximate correspondence between low scattering regions in OCM images and neuronal cell bodies. (c) Automated software segmentation and rendering of cell bodies from OCM data reveals three-dimensional neuronal architecture. (d) OCM cell density compared with TPM neuron and astrocyte density profiles, showing better agreement with neuron density profile. (e) Cell density and spacing profiles computed from OCM data. Unlike conventional histology, these profiles are obtained *directly* from three-dimensional data, and do not require stereological assumptions. (See [Media 1](#)).

2.4.2 Cell density

To obtain a measure of cell density as a function of depth, the 600 μm cubic volume was first partitioned into blocks of approximately 17.5 μm in depth. The cell depths (given by \bar{z}) were then used to register the cells to their corresponding blocks. The cell density was then computed by the number of cells per mm^3 . A histogram showing the cell density profile within the image volume, i.e., the number of cells at varying depths, was then constructed.

2.4.3 Cell spacing

The spacing between cells was quantified by first finding the minimum 3-D Euclidean distance between each cell in the volume and its nearest neighbor. The volume was again divided into a set of blocks, and the average of these minimum distances across all cells located within each particular block was determined. Cells at the boundaries of the imaged volume were excluded to avoid edge effects. A histogram of the average spacing between a cell and its nearest neighbor at varying depths was then constructed.

2.4.4 Myelin content

To quantify *en face* cortical myelin content, a depth-variant amplitude threshold (accounting for attenuation with depth due to scattering) was used. Voxels with amplitudes above the depth-variant threshold were designated as myelinated. The volume fraction was then calculated as the number of voxels with intensities above the threshold at a given depth divided by the total number of voxels at that depth. As explained in the Discussion section, only myelin fibers perpendicular to the optic axis can be visualized with OCM. The calculation was repeated on 50 coronal optical slices, and results from all coronal optical slices were averaged and plotted as a function of cortical depth.

3. Results

Figure 2(a)-2(b) shows two-photon microscopy (TPM) and Optical Coherence Microscopy (OCM) images of approximately the same transverse optical slice in a living rat. This validation step confirms that OCM indeed preferentially visualizes neurons relative to astrocytes. The neuronal cell bodies detected by OCM can be rendered in three-dimensions (Fig. 2(c), see also [Media 1](#)) to show cytoarchitecture. When OCM cell counts were compared with TPM neuron and astrocyte counts, the OCM cell counts agreed better with neuron counts than astrocyte counts (Fig. 2(d)). We attribute the drop in neuron and astrocyte densities measured by TPM beyond 250 μm to vessel shadowing and the limited penetration depth of TPM. The TPM astrocyte densities agree with previously reported values [18] up to 250 μm depth. Cell densities were not compared for depths of less than 60 μm because of surface artifacts. Densities or inter-cell spacings can also be computed directly from OCM volumetric data (Fig. 2(e)). Comparable cell densities and variations with depth have been reported in the literature [19].

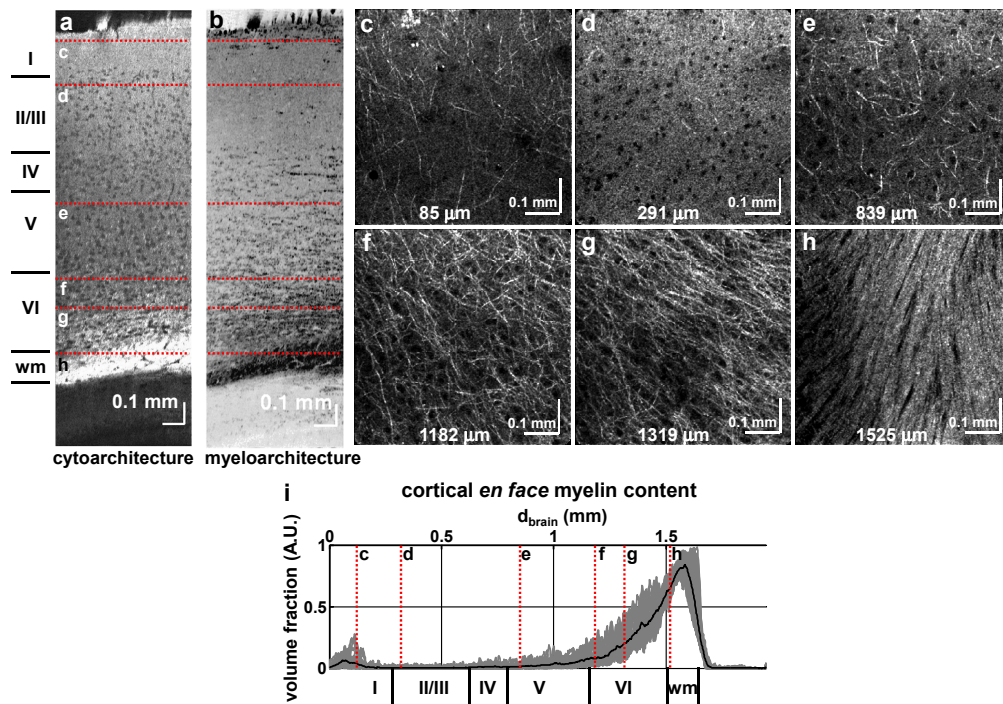


Fig. 3. OCM, when combined with *ex vivo* optical clearing techniques, depicts laminar cortical cytoarchitecture and myeloarchitecture in three-dimensions, over the entire cortical depth and beyond. The imaging geometry is shown in Fig. 1(a). (a) Cytoarchitecture is visualized with a minimum intensity projection. (b) Myeloarchitecture is visualized with a maximum intensity projection and displayed on an inverted colorscale. (c-h) Individual *en face* images in the transverse plane show the expected trends in cytoarchitecture and myeloarchitecture, with myelination increasing with cortical depth until the white matter (wm) is reached. (i) Quantification of cortical *en face* myelin content vs. depth confirms the trend of increasing myelination with depth as well as the cortical myelination in layer I (c). (Media 2)

Figure 3(a)-3(b) shows optical slices of cytoarchitecture and myeloarchitecture, obtained from volumetric OCM data acquired *ex vivo* from a mouse brain cleared with *Scale* solution (see also Media 2). Cytoarchitecture is visualized with a minimum intensity projection (Fig. 3(a)), while myeloarchitecture is visualized with a maximum intensity projection (Fig. 3(b)). To provide a view comparable to myelin silver stains, myeloarchitecture is viewed with an inverted color scale, thus darker regions in Fig. 3(b) contain more myelin. Figure 3(c)-3(h) show *en face* images (transverse optical slices) at specified depths, showing increasing myelination with increasing depth. Even the fine fibers in layer I, very difficult to visualize via myelin stains, are clearly depicted. The depth-dependent myelination profile is confirmed in Fig. 3(i). The mean volume fraction over 50 coronal optical slices is plotted in black, while individual coronal profiles are plotted in gray. While scale bars are dimensionally accurate, tissue swelling in the *Scale* solution was present [11], and cortical dimensions may not be anatomically accurate.

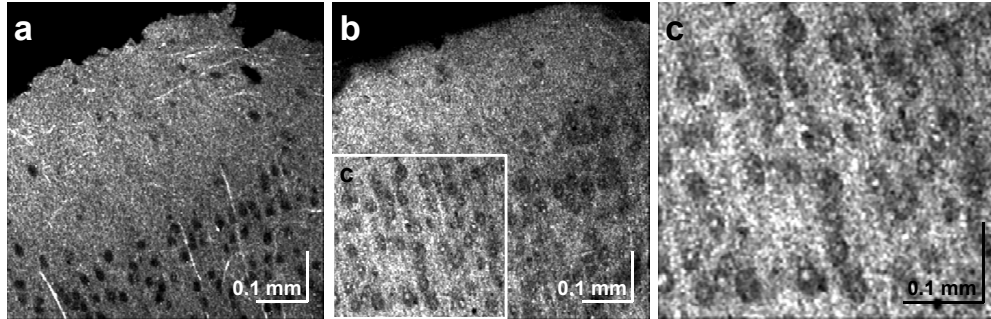


Fig. 4. Contrast mechanisms were investigated by application of acetic acid. (a) Image of a cleared mouse cortex cut along a coronal plane, imaged via the coronal surface (as shown in Fig. 1(b)). (b) Comparable image after application of acetic acid show highly scattering centers corresponding to the cell nuclei. Registration between (a) and (b) was not preserved due to tissue volume swelling after acetic acid application. (c) Zoom of boxed region in (b) reveals punctate scattering centers, resembling nuclei, surrounded by hyporeflexive regions, resembling soma. These results are consistent with the assertion that OCM, without the application of acetic acid, selectively visualizes the neuronal soma.

Figure 4 shows investigation of the origins of image contrast through application of acetic acid. *En face* coronal images of the brain via a cut coronal plane (Fig. 1(b)) near the cortical surface shows neuronal cell bodies (Fig. 4(a)). Addition of acetic acid results in cell swelling and the appearance of highly backscattering centers, which resemble the cell nuclei (Fig. 4(b)-4(c)). The appearance of the highly scattering nucleus surrounded by a low scattering region after application of acetic acid suggests that low scattering regions observed in OCM images are indeed neuronal cell bodies. These changes induced by acetic acid are consistent with nuclear coagulation reported previously in the literature [16].

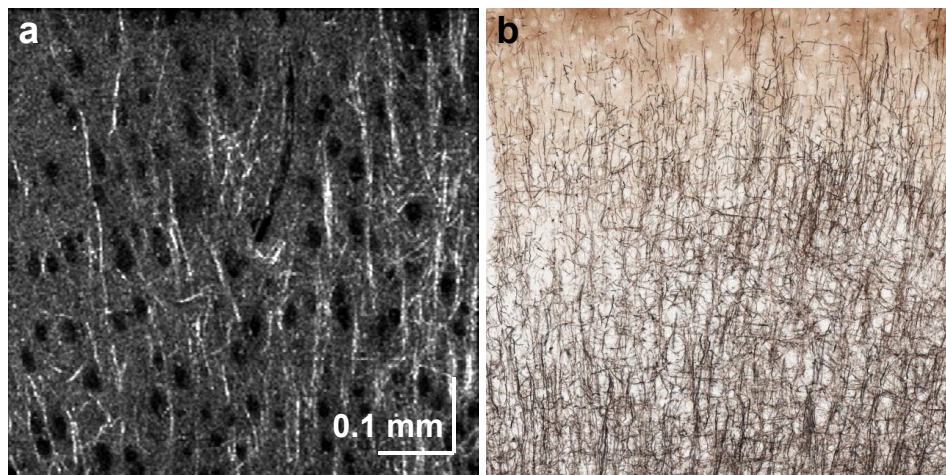


Fig. 5. (a) OCM contrast, derived from optical backscattering, is sensitive to imaging geometry. Imaging via a cut coronal plane (as shown in Fig. 1(b)) reveals vertically oriented cortical myelin fibers, as compared with Fig. 3, obtained by imaging via the cortical surface (as shown in Fig. 1(a)), which visualizes horizontally oriented myelin fibers. (b) Example image of a Gallyas myelin stain, taken from the same brain region. Retrieved from the Mouse Brain Architecture Project (<http://brainarchitecture.org/mouse/>), available under a Creative Commons Attribution-ShareAlike 3.0 Unported License.

The confocal imaging geometry defines an optic axis, as well as an *en face* plane perpendicular to the optic axis. As previously demonstrated [7], only backscattering from myelinated axons in the *en face* plane is clearly distinguishable from the background. Thus,

due to the directional backscattering of myelin fibers, certain orientations are preferentially visualized. When the brain is cut along a coronal plane and imaged via the cut face (Fig. 1(b)) vertical myelinated axons in layer II/III, perpendicular to the cortical surface, are visualized (Fig. 5(a)), providing a view similar to a conventional Gallyas myelin stain (Fig. 5(b)). These fibers are not visualized in Fig. 3 where, by virtue of the different imaging geometry (Fig. 1(a)), the same fibers are parallel to the optic axis.

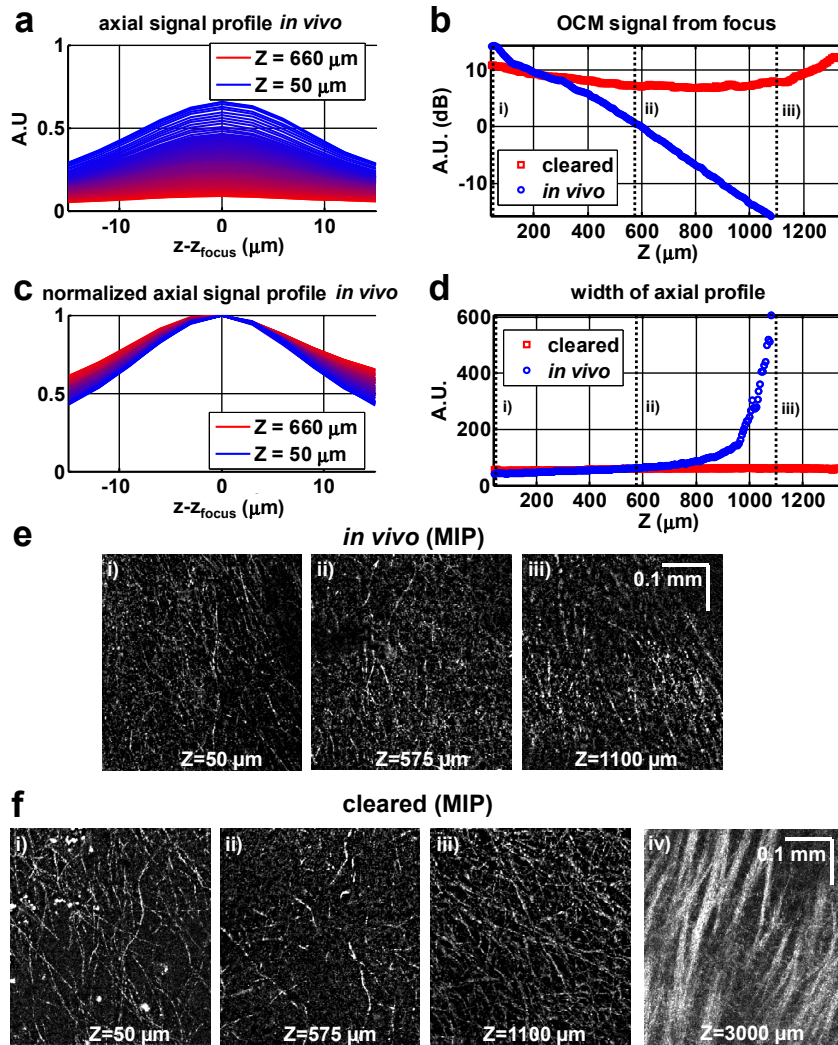


Fig. 6. A comparison of *in vivo* OCM without clearing and *ex vivo* OCM after clearing suggests that the clearing procedure reduces signal attenuation and blur. (a) *In vivo* axial signal profile around the focus demonstrates attenuation as the focus moves deeper in tissue. (b) With increasing focus depth, OCM after fixation and clearing reveals less attenuation of signal from the focus than *in vivo* OCM. (c) *In vivo* normalized axial signal profile demonstrates broadening as the focus moves deeper in tissue. (d) With increasing focus depth, OCM after fixation and clearing reveals less broadening of the axial signal profile than *in vivo* OCM. A broad axial signal profile is a possible indicator of detected multiple forward scattered light, which degrades image contrast. (e-f) In agreement with these observations, *in vivo* OCM contrast degraded at depths of ~ 1 mm, whereas *ex vivo* OCM with clearing revealed contrast at depths of ~ 3 mm (the maximum depth allowed by the working distance of our objective). Maximum intensity projection (MIP) images are shown to highlight myelinated axons. The imaging geometry is shown in Fig. 1(a).

In order to explore the mechanisms of contrast enhancement induced by optical clearing, *in vivo* OCM data acquired without clearing was compared to *ex vivo* OCM data acquired after fixation and chemical clearing (Fig. 6). One mouse brain was imaged *in vivo* through a closed cranial window, while another mouse brain was imaged *ex vivo* after fixation and *ScaleA2* clearing as described in Section 2.3. The two data sets were compared according to the OCM signal from the focus and the width of the axial signal profile around the focus as a function of sample arm assembly translation (Z). *In vivo* axial signal profiles around the focus (Fig. 6(a)) showed a characteristic attenuation with depth (blue circles in Fig. 6(b)), in agreement with our previous results in rats [7]. By comparison, *ex vivo* results (red squares in Fig. 6(b)) from the cleared mouse brain showed slight attenuation of OCM signal in the supergranular layers, transitioning to a growth in OCM signal with depth as cortical myelination (and reflectance) increased in layers IV-VI. The dramatically flatter signal plot achieved with optical clearing may be due to a reduction in attenuation from scattering [20]. Moreover, the width of the axial signal profile around the focus increased with focus depth *in vivo* (Fig. 6(c) and blue circles in Fig. 6(d)), whereas the axial signal profile width was roughly depth-invariant in the fixed brain after clearing (red squares in Fig. 6(d)). Increased width of the axial signal profile may be a hallmark of detected multiple forward scattered light, which degrades contrast deeper in tissue. In agreement with these observations, *in vivo* maximum intensity projection (MIP) images (Fig. 6(e)) exhibited degradation of image contrast with increasing depth. In the fixed, cleared brain (Fig. 6(f)), contrast was maintained and high resolution imaging down to ~ 3 mm depth was possible. Longer working-distance objectives may achieve even higher imaging depths.

4. Discussion

In this work, the use of optical clearing techniques to improve OCM penetration depth is demonstrated. In the context of fluorescence microscopy, refractive index mismatches are an obvious source of scattering and resolution loss, and should thus be minimized. Recently, hydrogel techniques that render the brain optically transparent and macromolecule permeable through removal of lipids were introduced [21, 22]. Removal of lipids is an ideal concept to optimize fluorescence brain imaging. However, to enhance the reflectance-based imaging methods presented here, one is compelled to take a more sympathetic view of scattering. On one hand, image contrast arises from refractive index mismatches – for example, the high refractive index of the lipid-rich myelin sheath, provided its refractive index is greater than the clearing solution, generates useful image contrast. On the other hand, the detection of multiply scattered light eventually limits the imaging depth. Hence, optical clearing in the context of reflectance-based imaging must strike a delicate balance between a loss of intrinsic contrast at one extreme, and a loss of penetration depth at the other. In this work, optical clearing enabled a dramatic improvement in penetration depth, enabling cellular-level, label-free imaging up to the ~ 3 mm working distance of our objective (Fig. 6(f)). The refractive index of the *ScaleA2* clearing solution (~ 1.38) was lower than the lipid refractive index, hence myelin was still visualized after clearing [23]. A chemical agent (acetic acid) was demonstrated to modulate image contrast (Fig. 4). Other treatments could potentially highlight different cellular or subcellular structures, or change scattering anisotropy in a beneficial way. We surmise that the most beneficial treatments would increase backscatter (detected signal) and reduce detection of forward scatter (contributing to image blur). Quantitative investigations of this hypothesis will be the subject of future investigations.

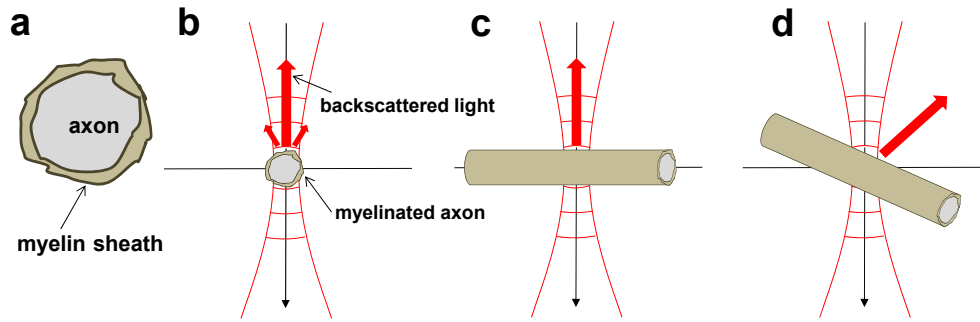


Fig. 7. (a) The lipid-rich myelin sheath has a higher refractive index than the cylindrical axon, leading to directional scattering properties. (b-c) If the axon is oriented in the plane perpendicular to the optic axis, backscattered light is detected along the optic axis (thick red arrow). (d) However, if the axon is oriented at an oblique angle, the amount of light that is backscattered and detected is reduced.

In addition to imaging results, techniques of quantifying cytoarchitecture and myeloarchitecture were demonstrated. In agreement with previous studies [7], our results show a closer correspondence between OCM cell densities and neuronal cell densities than astrocyte cell densities (Fig. 2(d)). Calculated neuronal cell densities in the rat cortex (Fig. 2(d)) are comparable with, though slightly lower than, counts from previous studies [19]. The lower counts observed here may be related to the fact the two-photon microscopy occasionally depicted apparent neuronal cell bodies that were not visualized by OCM (Fig. 2(a-b)) at shallow depths. Shadowing by superficial vasculature may also reduce OCM neuron counts. The preferential visualization of neuronal cell bodies relative to neurites by OCM suggests that the spherical soma and uniform intracellular refractive index profile leads to lower backscattering relative to the neurite background. Astrocytes may possess morphologies, sizes, and refractive index profiles that lead to comparable backscattering to the neurite background. While not explicitly shown here, our results suggest that other glia may possess backscattering properties more similar to astrocytes than neurons.

Our results suggest that OCM has the capability to image only myelinated axons in the *en face* or transverse plane (Fig. 3 and Fig. 5). These observations suggest the representation of light scattering shown in Fig. 7, where the higher refractive index of the myelin sheath leads to a directional scattering profile, dependent on the fiber orientation. Quantification of the subset of fibers located in the transverse plane leads to cortical myelination profiles (Fig. 3(i)), which can be used in the future as a baseline to investigate models of white matter injury. While, strictly speaking, we have not shown the capability to image myelin orientations in three dimensions, we anticipate that by rotating a cleared sample, as is routinely done in optical projection tomography [24], and obtaining volumes with different optic axis orientations, it will be possible to image and co-register multiple orientations of myelinated fibers in a three-dimensional volume.

Traditionally, myelin has been visualized by antibody immunohistochemistry (Luxol fast blue) as well as histochemical procedures such as the Gallyas stain [25]. However, these methods require tissue cutting and destructive impregnation procedures. Moreover, they cannot be used to determine connectivity, as they inherently provide two-dimensional projections. Electron microscopy [26] visualizes the myelin sheath, and in combination with ultramicrotomy enables tracing of myelinated axons over long distances [27]. However, these methods require extensive tissue processing, and may not scale favorably for imaging large volumes. Neuroanatomical tracer-based techniques, used for mesoscopic mapping, require hundreds to thousands of brains, with multiple injections per brain, to comprehensively determine connectivity [28]. Such methods have limited applicability in human subjects, where active transport of injected *in vivo* tracers is not possible. Moreover, *ex vivo*

intramembraneous passive diffusion of lipophilic dyes is too slow to visualize long range connectivity [29].

In comparison with the above methods, volumetric mapping of intrinsic optical contrast provided by the myelin sheath is applicable across species, and can potentially determine connectivity in a single brain without cutting or exogenous labeling. Therefore, the methods presented here have potential as tools for three-dimensional connectivity mapping. Finally, although a cortical volume of only $\sim 1 \text{ mm}^3$ was imaged here, in the future, we will investigate higher speed imaging methods [30] to achieve imaging volumes comparable to the complete mouse brain ($\sim 500 \text{ mm}^3$) [31]. The eventual long-term goal is to map all myelinated axons in the human brain.

5. Conclusion

In conclusion, Optical Coherence Microscopy (OCM), in conjunction with software focus-tracking and computational methods, was demonstrated to quantify brain architecture both *in vivo* and *ex vivo*. The methods of quantitative tissue characterization presented here have several advantages over conventional two-dimensional sectioning, mounting, staining, imaging, and stereological procedures [32]. In particular, metrics (cell density, size, shape, morphology, etc.) can be defined directly based on three-dimensional data, whereas assumptions are required to reconstruct inherently volumetric parameters from two-dimensional projections. Moreover, the fact that the techniques used here are label-free will enable more extensive studies of architectonic features over large volumes in samples where genetic labeling and immunostaining are either impossible or impractical. Combination with automated tissue slicing will extend the capability to image even larger tissue volumes [33]. Such studies will first require a systematic understanding of the origins of species-specific backscattering contrast in OCM images, as well as changes incurred by different fixation techniques and chemical treatments.

Acknowledgments

We acknowledge support from the National Institutes of Health (R00NS067050 and R01EB001954), the American Heart Association (11IRG5440002), and the Glaucoma Research Foundation Catalyst for a Cure 2. We thank Bruce Rosen and Maria Angela Franceschini for general support.